

In situ visualization and real-time tracking of emulsion and miniemulsion polymerization at the microscale via fluorescence imaging

Haotian Liu ^{a,b}, Jie Shi ^{a,b}, Yuan Pu ^b, Jie-Xin Wang ^{a,b}, Dan Wang ^{a,b,c,*}, Jian-Feng Chen ^{a,b}

^a State Key Laboratory of Organic-Inorganic Composites, Beijing University of Chemical Technology, Beijing 100029, China

^b Research Center of the Ministry of Education for High Gravity Engineering and Technology, Beijing University of Chemical Technology, Beijing 100029, China

^c Harvard John A. Paulson School of Engineering and Applied Sciences, Harvard University, Cambridge, MA 02138, USA

HIGHLIGHTS

- *In situ* visualization of polymerization was achieved by fluorescence imaging.
- Unique phase separation phenomenon was observed during miniemulsion polymerization.
- Superhydrophobic fluorescent nanoparticles were synthesized in rotating packed bed.

ARTICLE INFO

Article history:

Received 25 July 2019

Received in revised form 5 October 2019

Accepted 12 October 2019

Available online 31 October 2019

Keywords:

In situ visualization

Emulsion and miniemulsion polymerization

Polystyrene nanoparticles

Fluorescent imaging

Aggregation induced emission

ABSTRACT

We report a simply designed liquid sample cell to visualize the processes of emulsion and miniemulsion polymerization by real-time fluorescence imaging of aggregation-induced emission fluorogens (AIEgens) in the emulsions. A unique phase separation phenomenon was observed in the styrene droplets during miniemulsion polymerization, which is beneficial for surface engineering of the polymer nanoparticles. Accordingly, a process intensified synthesis approach to polystyrene (PS) nanodispersion via emulsifier-free miniemulsion polymerization was developed in rotating packed bed reactors. Superhydrophobic fluorescent PS nanoparticles are fabricated via a cost-effective approach and exhibited a water/air contact angle of over 155°, which are promising for fluorescent liquid marbles. These findings not only provide the basis for real-time tracking and characterization of polymerization processes at the microscale via fluorescence imaging of AIEgens, but also offer a new route for the cost-effective production of superhydrophobic polymer nanoparticles for advanced applications.

© 2019 Elsevier Ltd. All rights reserved.

1. Introduction

Emulsion polymerization, a crucial preparation technique of polymeric nanoparticles, is widely employed for the synthesis of complex structured polymeric nanoparticles, nanocapsules with polymer shells and polymeric Janus particles (Fan et al., 2017; Hejmady et al., 2019; Huang et al., 2017; Landfester, 2009). Typically, polymer particles are formed by micellar nucleation in emulsion polymerization (Sajjadi and Jahanzad, 2006) and the particle structure can be varied by choosing different surfactants, as shown by previous studies (Rao and Geckeler, 2011). However, a large quantity of surfactant is required to keep the micelles stable. The extra surfactant raises the product cost and reduces the product performance if it is not completely removed. In the recently devel-

oped miniemulsion polymerization technology, which avoids the use of extra surfactants, the droplets in the emulsion act as tiny reactors that limit the amount of reactive monomer necessary to form the particle (Castor et al., 2015; Jiang et al., 2014; Liu et al., 2019). However, the particles produced by miniemulsion polymerization are usually much larger than those obtained from emulsion polymerization (Gharieh et al., 2019). Another study showed that the change in droplet phase state during polymerization is a complex process (Truong et al., 2017). There are intermediate states when the liquid droplets transform into solid particles. The phase transformation process of polymerization plays a significant role in the structure formation of the particle (Drache et al., 2018; Thickett and Teo, 2019). Therefore, knowledge of *in situ* visualization and real-time tracking of emulsion and miniemulsion polymerization processes at the microscale is critical to develop new approaches for the preparation of polymer nanoparticles with uniform size distributions (Asua, 2014; Sacci et al., 2014; Zhang et al., 2015; Neuville et al., 2017).

* Corresponding author at: State Key Laboratory of Organic-Inorganic Composites, Beijing University of Chemical Technology, Beijing 100029, China.

E-mail address: wangdan@mail.buct.edu.cn (D. Wang).

In contrast with the expensive and sophisticated *in situ* transmission electron microscopy (TEM) technique, laser scanning confocal microscopy (LSCM) and atomic force microscopy (AFM) are widely used techniques for *in situ* visualization in biology and materials science (Fukui et al., 2018). AFM has been used to visualize the dynamics of many biological and chemical systems due to its extraordinary spatial resolution (Hans et al., 2009; Pyun et al., 2005; Zhang et al., 2016). Unfortunately, the accurate visualization facility that characterized the solid products formed in these systems is incapable of studying phase transitions. Owing to the synthesis of diverse functionalized fluorescent probes, LSCM has been a powerful strategy for biological and chemical process visualization. Traditional chromophores are not ideal fluorescent probes for sustained observation because of the aggregation-induced quenching and photobleaching phenomena in the solid state. When aggregation-induced emission fluorogens (AIEgens) were first reported by Tang in 2001, the problems mentioned above were resolved (Hong et al., 2009; Mei et al., 2015). Henceforth AIEgens with low background noise were widely applied in the continuous monitoring of biological processes (Qin et al., 2012; Zhao et al., 2016; Huang et al., 2016; Yuan et al., 2014). Furthermore, AIEgens were applied for the real-time monitoring of chemical reactions (Leung et al., 2016). A common method to visualize a chemical reaction employs the strong emission caused by AIEgens in the aggregated state which attach directly to the reactants during the reaction (Guan et al., 2016; Tian et al., 2019). This precise location of the dye molecules can show the segmental motion of the polymer but barely affects the intrinsic properties of the polymers (Liu et al., 2018). Therefore, the *in situ* label merely provides an insight into the process at the molecular level rather than into the system as a whole.

In this work, we designed a liquid sample cell that has a simple structure, fewer parts and easy fabrication. The sample cell is used to visualize the formation process of polymer particles in emulsion and miniemulsion polymerization by confocal laser scanning microscopy (CLSM). The AIEgens were employed as fluorescent probes to specifically label the droplet phase state during the polymerization process. The principle of polymerization process visualization was based on the AIEgens aggregated state caused by the increase in viscosity of the local environment. The light-induced emulsion polymerizations of polystyrene (PS) using styrene as the monomer and encapsulation in the liquid sample cell were investigated in real-time by CLSM. *In situ* real-time fluorescence imaging showed the characteristics of the emission and miniemulsion polymerization processes and indicated that the droplet size is an important factor in miniemulsion polymerization. A high-gravity emulsifier-free miniemulsion polymerization approach for the synthesis of PS nanodispersions based on the use of a rotating packed bed (RPB) reactor was proposed to obtain PS nanoparticles with uniform size. Furthermore, the proposed *in situ* method for real-time visualization of the miniemulsion polymerization process inside the liquid sample cell could disclose a previously unknown aggregation and morphology

in polymerized droplets. Fluorescent nanoparticles doped with low-dose aminopropylisobutyl polyhedral oligomeric silsesquioxane (POSS-NH₂) on the surface were synthesized based on the phenomenon of phase separation, and their preliminary application for liquid marbles was demonstrated.

2. Experimental section

2.1. Materials

Styrene (St) was purchased from Aladdin Industrial Corporation and was passed over basic alumina to remove inhibitors prior to use. Sodium dodecyl sulfate (SDS), chloroform, tetrahydrofuran (THF), 2,2'-azobis(2-methylpropionitrile) (AIBN), camphorquinone (CQ), ethyl 4-dimethylamino benzoate (EDMAB) and 1,1,2,3,4,5-hexaphenylsilole (HPS) were purchased from Sigma-Aldrich. Basic information on CQ and HPS is shown in the [Supplementary Information](#) (Fig. S1), including the UV-vis absorption spectra and chemical structures. Aminopropylisobutyl polyhedral oligomeric silsesquioxane (POSS-NH₂) was purchased from Hybrid Plastics. All the chemicals were used without any additional purification unless specifically mentioned. Instant adhesive CA40H was purchased from 3 M. Kapton® Type 100HN films were purchased from DuPont. Glass slides and coverslips were purchased from Citotest. Deionized water obtained using a laboratory water purification system was used for all experiments.

2.2. Preparation of styrene emulsion

As a typical recipe, 2.0 g of St, 0.25 mg of HPS, 10.0 mg of CQ and 40.0 mg of 4-EDMAB were stirred together in a 10 mL beaker at 0 °C and in a dark place for 10 min, forming a homogeneous solution (solution A). Meanwhile, 20 mg of SDS was dissolved in 40 mL of water, forming a homogeneous solution (solution B). For the emulsion process, solution A and B were mixed using a high-speed dispersion homogenizer (Ultra-Turrax, IKA T18 digital) for 60 s at 15 krpm. The emulsion was maintained at 10 °C and kept in a dark place to prevent polymerization.

2.3. Fabrication of liquid sample cell

The liquid sample cell consisted of a simple structure, composed of a glass slide, gaskets and a coverslip (Fig. 1). Briefly, Kapton® Type 100HN film (25 µm thick) was fragmented into strips (3 × 22 mm), which were used as the gaskets to regulate the distance between the glass slide (25 × 75 mm) and the coverslip (22 × 22 mm). Two gaskets were laid on either side of the coverslip and covered tightly by the glass slide. The interfaces of the gasket were sealed with the instant adhesive CA40H at 60 °C. The distance between the glass slide and coverslip can be adjusted by the thickness of the gasket.

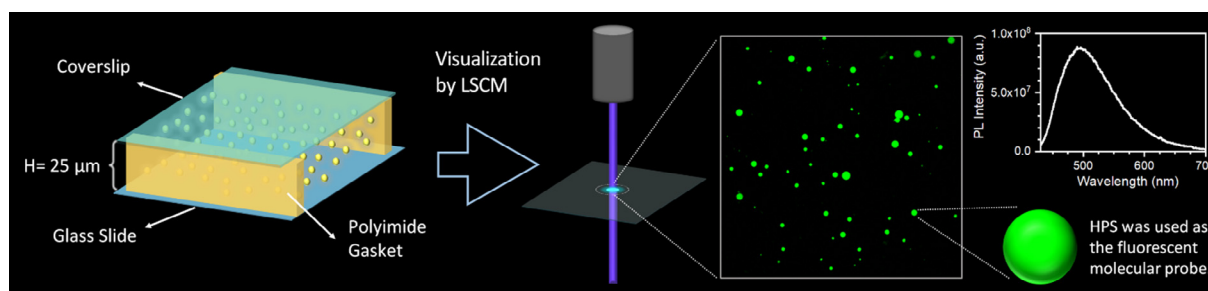


Fig. 1. Schematic representation of liquid sample cell and visualization of styrene emulsion in liquid sample cell by CLSM. The inset shows the PL spectrum of HPS. $\lambda_{\text{ex}} = 405 \text{ nm}$, $\lambda_{\text{em}} = 435\text{--}700 \text{ nm}$.

2.4. Sample loading and fluorescent visualization

The emulsion was loaded into the liquid sample cell from the unsealed flanks based on the capillary phenomenon. The loading process needs to be repeated several times in order to exclude bubbles from the cell. After removing excess emulsion with filter paper, the flanks were sealed with the instant adhesive CA40H. The sealed cell was kept in a dark place at 4 °C for 2 h, allowing complete solidification of the adhesive. The liquid sample cell was then imaged by CLSM (TCS SP8, Leica, Germany) upon excitation by 405 and 488 nm laser, and the fluorescent signals were collected at a wavelength above 500 nm (Fig. 1). Time-dependent confocal images of the cell were collected for a total irradiation time of 16.5 min by CLSM, using the following parameters: scan speed = 400 Hz; zoom = 1.1; pinhole size = 1 AU; intensity of 405 nm laser line = 15%; intensity of 488 nm laser line = 20%. Fluorescence images were collected by the PMT1 detector from channel 1 at 500–560 nm. Bright images were collected by the PMT trans detector from the transmission channel.

2.5. Synthesis of PS particles

The synthesis of PS nanoparticles by RPB miniemulsion polymerization was conducted by a two-step process composed of emulsification and miniemulsion polymerization (Fig. S5). Briefly, 10 g of St and 500 mg of AIBN were stirred together in a 20 mL beaker at 15 °C for 10 min, forming a homogeneous solution (solution A). For the emulsification process, solution A and 100 mL of water were pumped into a RPB reactor via two inlets at liquid flow rates of 5 mL/min and 50 mL/min, respectively. Then the emulsion was circulated between the RPB reactor, tubular heat exchanger and stirred reactor for miniemulsion polymerization. The temperature of the emulsification system was controlled at 20 °C during the miniemulsion process and the microemulsion was then circulated at 80 °C for 2 h, allowing complete polymerization of the reactants to form nanoparticles. The classical emulsion and miniemulsion polymerization of styrene were conducted by one-step processes. In miniemulsion polymerization, 10 g of St and 500 mg of AIBN were mixed in a flask and 100 mL of deionized water was added for emulsification. After stirring for 10 min at room temperature, the emulsion was heated at 80 °C for 8 h. The PS nanoparticles were synthesized by emulsion polymerization via the same process, but 100 mL of 20 mg/mL SDS aqueous solution was added instead of deionized water for emulsification. To assess the effect of POSS-NH₂ on the surface performance of PS nanoparticles, POSS-NH₂:HPS@PS nanoparticles were synthesized via the same process of RPB miniemulsion polymerization. For this synthesis, 10 g of St, 500 mg of AIBN, 20 mg of HPS and 300 mg of POSS-NH₂ were stirred together in a 20 mL beaker at 15 °C for 10 min (solution A). Other experimental parameters were the same as for the synthesis of PS nanoparticles by RPB miniemulsion polymerization.

2.6. Characterization

The polymer molecular weights were determined by gel permeation chromatography (GPC, 1515GPC, Waters, America) analysis. The Fourier transform infrared (FTIR) spectra were obtained using a PerkinElmer Spectrum GX FTIR spectroscopy system in the range of 400–4000 cm⁻¹. X-ray photoelectron spectroscopy (XPS) measurements were performed on a VG Microtech ESCA 2000. The morphologies of the POSS-NH₂:HPS@PS and PS nanoparticles were observed by a Hitachi HT7700 transmission electron microscopy (TEM) at an accelerating voltage of 100 kV and a JEOL *JSM-7800F scanning electron microscope (SEM) at an accelerating voltage of 10.0 kV. The absorption spectra were obtained using a Shimadzu UV-2600 spectrometer. The fluorescence spectra were

recorded using an Edinburgh Instruments FS5 fluorescence spectrometer with an excitation wavelength of 405 nm. The conversion of styrene was determined using a gas chromatography (GC) system (Shimadzu GC-2014C, N₂ as the carrier gas, a flame ionization detector (FID) and a chromatographic column of GsBP-Plot Al₂O₃ (100 m × 0.53 mm × 15 μm)). The temperatures of the injector and FID detector were 80 and 250 °C, respectively.

2.7. Calculation methods

First-principles calculations based on spin-polarized density-functional theory (DFT) were performed using DMol3 code. Hybrid density functional B3LYP in combination with double numerical basis sets with polarization functions (DNP) were used to calculate nonlocal gradient corrections to the correlation and exchange energies (Becke, 1993; Delley, 2006; Stephens et al., 1994). All electrons are included in the calculation. To be more precise, the self-consistent field (SCF) convergence accuracy was increased to 1.0×10^{-6} Ha. The convergence thresholds for energy, force, and displacement were set to be 1.0×10^{-5} Ha, 0.002 Ha/Å, and 0.005 Å, respectively. We used a 0.005 Ha smearing on electronic orbital occupancy and the global orbital cutoff was 3.7 Å, simultaneously. For other parameters, the default settings were taken.

3. Results and discussion

Photoinitiated CQ–EDMAB polymerization occurs through electron/proton transfer (Alvim et al., 2007). Irradiation of CQ with visible light causes the formation of triplet state CQ (Cook, 1992; Jakubiak et al., 2003). Triplet state CQ then abstract hydrogen from EDMAB (hydrogen donor), forming CQ and EDMAB primary radicals (Fig. 2A). The E_{HOMO} and E_{LUMO} showing the photoreactive activity of the CQ carbonyl group are shown in Fig. 2B. The calculation results indicated that the formation of triplet state CQ requires more than 1.90 eV of energy (Eq. (1)). In the experiment, the polymerization was triggered by a 488 nm laser (Fig. S1B, the absorption spectrum of initiator CQ). The quantum energy of light with a wavelength of 488 nm is 2.53 eV (Eq. (2)), which is enough to excite CQ molecules. The average kinetic energy of the molecule at 300 K is 0.04 eV (Eq. (3)), which has little effect on the photoinitiation process. The Fukui field calculation result showing the radical attack activity of the carbonyl group (Fig. 2C).

$$\Delta E_{\text{PBE}} = E_{\text{LUMO}} - E_{\text{HOMO}} = 0.0699 \text{ Ha} = 1.90 \text{ eV} \quad (1)$$

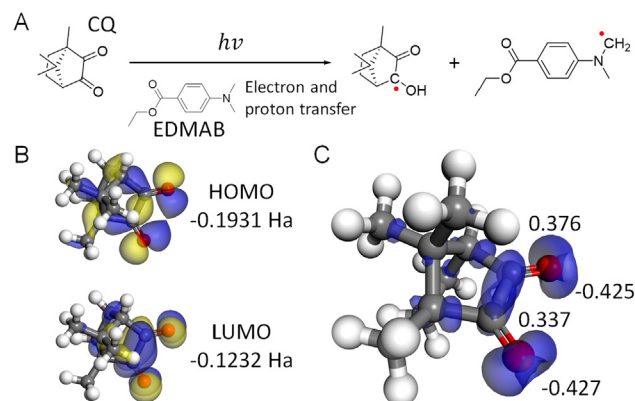


Fig. 2. (A) Formation of CQ and EDMAB primary radicals. The red dots represent the active atom. (B) Highest occupied molecular orbital (HOMO) and lowest unoccupied molecular orbital (LUMO) for CQ. The calculations were performed by the Perdew-Burke-Ernzerhof (PBE) function. (C) Fukui radical field; greater values indicate a greater susceptibility to radical attack. The iso-value for surfaces is 0.03. The insets are the electrostatic potential (ESP) charges of crucial atoms.

Table 1
SPIN of active atom and E_{banding} of primary and monomer radicals.

Name	CQ primary radical	CQ-St monomer radical 1.0	CQ-St monomer radical 2.0	EDMAB primary radical	EDMAB-St monomer radical 1.0	EDMAB-St monomer radical 2.0
Structure						
Spin of active atom	0.553	1.005	0.702	0.791	1.023	0.720
E_{banding} (eV)	–	1.1460	–0.0537	–	–0.1425	–0.6849

$$\varepsilon_{488} = hc/\nu = 4.073 \times 10^{-19} J = 2.53 \text{ eV} \quad (2)$$

$$\bar{\varepsilon}_k(300K) = 3kT/2 = 6.21 \times 10^{-21} J = 0.04 \text{ eV} \quad (3)$$

The generated CQ and EDMAB primary radicals react with the monomer to form monomer radicals, which initiate the polymerization reaction. The spin polarization calculation results of the primary and monomer radicals show the spin distribution of the radical system and determine the position of the active atom. The spin values of the radicals' active atoms show the transfer of spin during the polymerization process (Table 1). The calculation of the E_{banding} of monomer radicals is performed by Eq. (4). The calculation results indicate that the 1.0 structure of the CQ-St monomer radical has the strongest reactivity (Table 1, $E_{\text{banding}} = 1.1460$ eV). The Fukui radical fields of the primary and monomer radicals indicate that the monomer radicals have a higher reactivity (Fig. S2). The calculation results are confirmed by the characteristics of the chain-initiated process of free radical polymerization.

$$E_{\text{banding}} = E_{\text{product}} - E_{\text{radical}} - E_{\text{St}} \quad (4)$$

Emulsion and miniemulsion polymerization were triggered in the liquid cell and imaged by CLSM. In the nucleation process of miniemulsion polymerization, each droplet is an independent reaction unit in which polymerization occurs. Droplets with a

small range of movement for easy tracking during the reaction are observed for about 16 min during polymerization. In the video of miniemulsion polymerization captured using confocal imaging (Video S1), the transformation of styrene droplets can be clearly observed. The styrene droplets were marked as Obj.1 to Obj.21 in our experiment and tracked to characterize the transformation process in miniemulsion polymerization (Fig. S3, enlarged confocal images of the 21 styrene droplets). In the bright field image, the diameter of the styrene droplets gradually shrinks as polymerization proceeds. At the same time, the fluorescence intensity of the droplets in the dark field image gradually increases. The droplet fluorescence localization coincided with the bright field image, indicating that HPS is an ideal fluorescence probe for the emulsion polymerization system (Video S1, Merge). The fluorescence signal from HPS remained almost unchanged after continuous scanning for 400 times with a total irradiation time of ≈ 17 min, indicating its excellent photostability (Fig. S4).

The localization and diameter of the styrene droplets varied during the reaction. The confocal images of the objects at five time nodes are shown in Fig. 3A to demonstrate the variation of positioning. It is necessary to track the droplets frame by frame to ensure data accuracy. The diameter shrinkage ratio and average fluorescence intensity of the droplet reflect the reactant conversion and local environment viscosity, respectively. The fluorescence intensity is

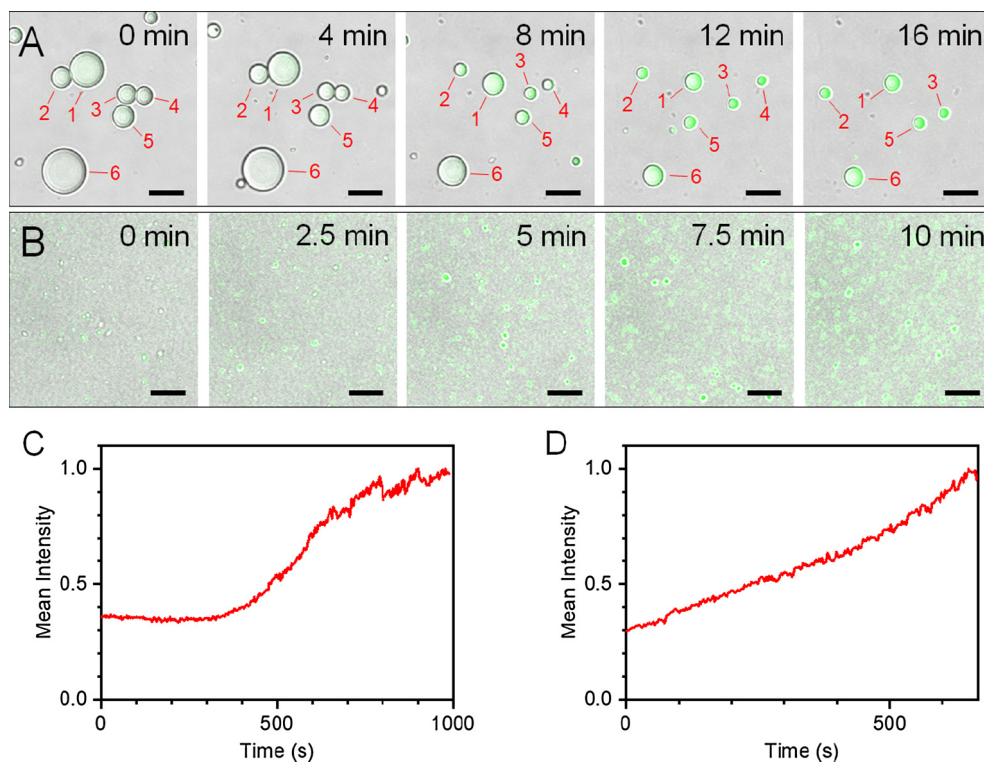


Fig. 3. (A) Confocal images of styrene miniemulsion polymerization for the total irradiation time from 0 to 16 min. (B) confocal images of styrene emulsion polymerization for the total irradiation time from 0 to 10 min. All images share the same scale bar (5 μm). (C) Normalized frame mean intensity of miniemulsion polymerization during reaction. (D) normalized frame mean intensity of emulsion polymerization during reaction.

Table 2

Analysis of styrene emulsion confocal images in Fig. 3A.

Time	0 min		4 min		8 min		12 min		16 min	
Obj.	Diameter μm	Avg. Intensity gray values	Diameter μm	Avg. Intensity gray values	Diameter μm	Avg. Intensity gray values	Diameter μm	Avg. Intensity gray values	Diameter μm	Avg. Intensity gray values
1	5.59	19.39	5.21	22.82	3.51	80.32	2.62	237.18	2.50	252.76
2	3.38	16.30	3.10	18.02	2.10	72.60	1.71	223.56	1.59	251.63
3	3.11	17.18	2.87	18.06	1.90	86.72	1.47	249.99	1.38	255.00
4	2.84	12.80	2.49	17.17	1.76	49.08	1.34	239.13	1.29	244.53
5	3.53	18.08	3.33	21.80	2.17	87.49	1.74	246.48	1.65	254.44
6	7.07	6.24	6.84	6.82	4.62	19.57	3.22	102.43	2.97	226.27

measured based on the gray-scale value, and the value range is from 0 to 255. The diameter and average fluorescence intensity of the observation objects were measured every 20 s. The measured data of the objects in Fig. 3A are given in Table 2. In addition, the detailed data acquisition process is demonstrated in Video S2.

Particle formation in emulsion polymerization occurs through micellar nucleation at the initial reaction stage. Due to its limited resolution, CLSM is unable to track the reaction process of individual polystyrene particles. Emulsion polymerization is characterized by the frame mean intensity as a function of time. In the video of emulsion polymerization captured by confocal imaging (Video S3), the fluorescence intensity of the frame increases with polymerization. The confocal images of emulsion polymerization at five time nodes are shown in Fig. 3B to demonstrate the variation of fluorescence intensity. The normalized frame mean intensity of emulsion polymerization has a linear relationship with time (Fig. 3D). In contrast, the normalized frame average intensity of miniemulsion polymerization has an S-curve relationship as a function of time (Fig. 3C). This is similar to the data for a single droplet in miniemulsion polymerization (Fig. 4A).

To facilitate comparison among the reactant conversions of different droplets, the diameter data were converted into diameter

shrinkage ratios. The relationship between shrinkage ratio and average intensity versus time is two S-curves that can be matched to the DoseResp function (Eq. (5)) (Fig. 4A). Detailed data related to the fitting results are given in the [supplementary information](#). Then, through the time derivation of the DoseResp function fitting result, the shrinkage rate and average intensity change rate curve were obtained (Fig. 4B). Similarly, the rate of change curves for shrinkage ratio and average intensity represent the change rate of reactant conversion and local environmental viscosity, respectively. In the early stage of polymerization, polymer chain concentration is low, droplet viscosity is small, and molecular movement is intense. Free radicals in the droplets are prone to collisions that cause chain growth to terminate. As the polymer concentration increases, the viscosity of the system increases and molecular motion slows down. The radical life is extended and the reaction rate gradually increases. Subsequently, a firm polymer network forms in the droplets at high conversion, which hinders the diffusion of free radicals and slows down the reaction rate. Due to the small droplet size, the reaction rate first increases and then decreases. The droplet viscosity is generally considered to be linear with the reaction rate. However, the local environmental viscosity of the droplets generally increases abruptly at a certain point in the

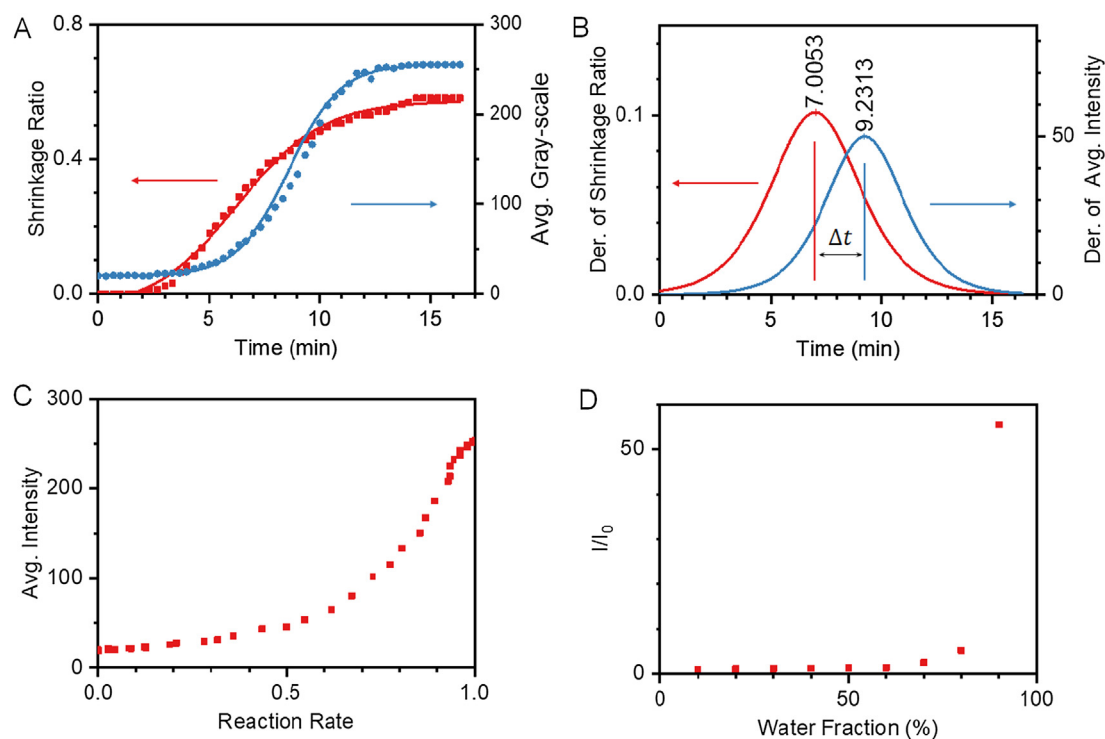


Fig. 4. (A) Plot of shrinkage ratio and average intensity versus time data of Obj. 1. The data were fitted by the DoseResp function. (B) The time derivation of shrinkage ratio and average intensity versus time data of Obj. 1. (C) Plot of average intensity versus reaction rate of Obj. 1. The detailed analysis data of the other 20 objects are given in the supporting information. (D) Plot of I/I_0 versus the water fraction of HPS. Concentration = 10×10^{-6} M; I_0 = PL intensity in pure tetrahydrofuran solution; λ_{ex} = 405 nm.

reaction and continues to grow rapidly for a period of time at the end of the reaction (Fig. 4C). This special phenomenon can be observed during the reaction of other droplets (Figs. S8–S27). The increase in abnormal viscosity is also inconsistent with the increase in fluorescence intensity caused by a decrease in solvent content (Fig. 4D).

$$y = A_1 + \frac{A_2 - A_1}{1 - 10^{(\text{Log}x_0 - x)p}} \quad (5)$$

A phase separation process is proposed to elucidate the abnormal increase in the local environmental viscosity of polymer droplets and related experimental results. Phase separation is a common phenomenon in concentrated styrene-polystyrene solutions because of the poor dispersion of the molecular structure of long polystyrene chains. There are two phases in a system with phase separation: a dilute phase and a thick phase. The thick phase contains more polymer molecules, resulting in a higher viscosity than that of the dilute phase. This can result in a heterogeneous distribution in the system and an anomalous increase in local environmental viscosity. We believe that there are two stages in the polymerization of droplets (Fig. 5A). Droplets are homogeneous systems of symmetrical local environmental viscosity in the early stages of polymerization. The droplet viscosity increases steadily with the reaction (Fig. 4C). When the polystyrene concentration reaches a critical value, instantaneous phase separation results in a significant increase in the local environmental viscosity of the droplets. The thick phase of the droplet then gradually expands as the reaction progresses, and the viscosity of the system continues to increase rapidly. In response to this, the droplet fluorescence intensity increases rapidly until the end of the reaction.

The anomalous increase in signal growth rate was investigated by calculating the time difference between the peaks of the rate of change curves of the shrinkage rate and the average intensity (Fig. 4B, Δt). Droplet diameter, the only difference between droplets, was used to measure different droplet systems. The right half width of the change curve for shrinkage ratio is used to measure

the length of the second half of the reaction of the individual droplets. The data indicated that there is no correlation between the temporal difference (i.e. the reason for the anomalous increase) and the individual size of droplets (Fig. 5B). This result excludes the influence of individual differences. Meanwhile, the right half width is highly correlated with the temporal difference, and the Pearson correlation coefficient is 0.46 (Fig. 5C). The reaction rate in the second half is the decisive factor affecting the time required for the polymer solution to reach the critical concentration. The earlier the polymer concentration reaches the critical value, the earlier the phase separation phenomenon will occur.

In situ visualization data indicate that droplet size affects the particle size and macroscopic reaction rate during miniemulsion polymerization. When the droplets in the system are small enough, the macroscopic conversion rate curve of the miniemulsion polymerization is similar to that of emulsion polymerization. At the same time, particles having a small size and a uniform size distribution can be obtained. The rotating packed bed (RPB) has been developed as an efficient apparatus to enhance the mass transfer of mixing of the reactants for various reactions (Liu et al., 2019; He et al., 2019; Wang et al., 2019). In our work, the RPB was used for miniemulsion polymerization to keep the emulsion droplets small and uniform in size during the reaction, in comparison to those performed in a conventional stirred reactor. Fig. 6A–C show the TEM images and the size distribution of PS particles prepared by three kinds of processes, namely miniemulsion polymerization, RPB miniemulsion polymerization and emulsion polymerization, respectively. RPB miniemulsion polymerization can be used to prepare nano-sized PS particles with an average diameter of 71 nm. Under the same conditions, PS particles prepared by miniemulsion polymerization had an average diameter of 1.1 μm . The polymer particles prepared by RPB miniemulsion polymerization have a more concentrated size distribution than those prepared by emulsion polymerization. The molecular weight of PS nanoparticles prepared by RPB miniemulsion polymerization determined by GPC was $M_w = 460,562$ Da. This is not only much higher than that of the PS particles prepared by

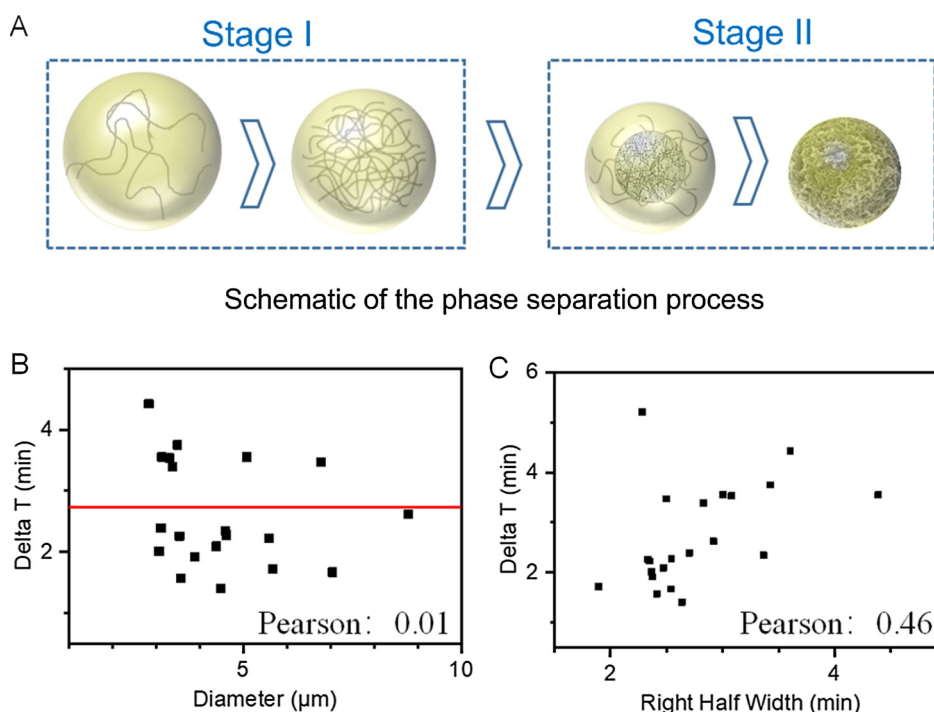


Fig. 5. (A) Schematic of the styrene emulsion polymerization process. (B) Plot of delta T versus diameter of Obj. 1 to 21. (C) Plot of delta T versus right half width of Obj. 1 to 21. The red inset line was the average of delta T.

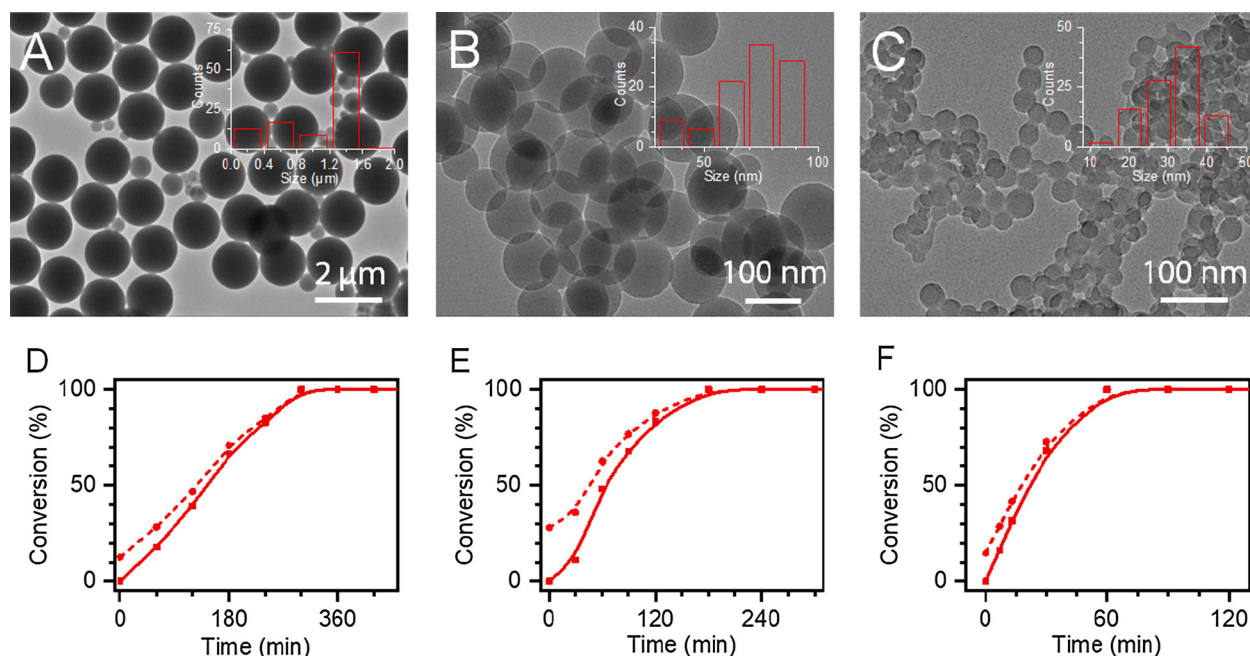


Fig. 6. TEM images of PS particles prepared by (A) miniemulsion polymerization, (B) RPB miniemulsion polymerization and (C) emulsion polymerization. The inset shows the size distribution of PS particles. Reaction conversion rate of styrene with (D) miniemulsion polymerization, (E) RPB miniemulsion polymerization and (F) emulsion polymerization versus time.

miniemulsion polymerization ($M_w = 83,320$ Da), but also higher than that of particles prepared by emulsion polymerization ($M_w = 336,769$ Da). As expected, the styrene conversion curve of miniemulsion polymerization is similar to that of emulsion polymerization, due to the reduction in the emulsion droplet size (Fig. 6D–F). The small size of the emulsion droplets not only inhibits free radical quenching of each reaction unit, but also substantially increases the number of effective reaction units in the system. This allows the reaction system to have some micelle nucleation characteristics and causes the RPB miniemulsion polymerization technique to have similar reaction characteristics to emulsion polymerization without surface activity.

Surface modification with low-dose modifier could be implemented via the phase separation phenomenon. The molecules, which had poor compatibility with long polymer chain structure, were beneficial in the dilute phase during polymerization. These molecules gather on the surface and influence the surface properties of the polymer particles formed. Aminopropylisobutyl polyhedral oligomeric silsesquioxane (POSS-NH₂), which can dissolve in styrene but is not compatible with the polystyrene chain structure, was used at a low dose (3 wt% of styrene) for surface-modification to decrease the wettability of polystyrene (PS) nanoparticles. The POSS-NH₂/HPS@PS nanoparticles exhibited a similar spherical shape as PS nanoparticles (Fig. 7A&B), and no surface defects were found on the nanoparticles doped with low-dose POSS-NH₂ (Fig. 7A, inset). The agglomeration interaction of the particles was attributed to the drying process in the preparation of the powder for SEM observation. Furthermore, no characteristic peak of POSS-NH₂ was found in the Fourier-transform infrared (FT-IR) and XPS spectra of POSS-NH₂@PS because of the low-dose modifier (Fig. S7A–C). The contact angles of PS nanoparticles were significantly increased when modified by POSS-NH₂, indicating that the low-dose POSS-NH₂ gathered on the surface of the PS nanoparticles (Fig. 7C, Fig. S7D). The modified PS nanoparticles can be used as shell material for preparing fluorescent liquid marbles (Fig. 7D). Compared to the high amount of modifier used in conventional surface modification, this modification method could realize stable surface modification with tremendous molecular use efficiency.

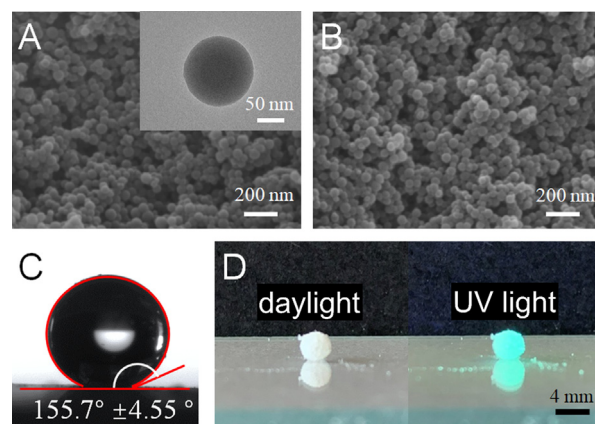


Fig. 7. SEM images of (A) POSS-NH₂/HPS-PS nanoparticles and (B) PS nanoparticles. The inset shows the TEM image of a POSS-NH₂/HPS-PS nanoparticle. (C) Contact angle photo of POSS-NH₂/HPS-PS nanoparticles; (D) Digital photos of liquid marbles made with POSS-NH₂/HPS-PS nanoparticles containing 0.35 mL of water, under daylight and under UV light. $\lambda_{ex} = 365$ nm.

4. Conclusion

In summary, we demonstrated the use of AIEgens for the *in situ* visualization and real-time tracking of emulsion and miniemulsion polymerization inside an easy fabrication liquid sample cell. This technique enabled us to get the *in situ* information on the emulsion and miniemulsion polymerization processes directly. *In situ* fluorescence imaging showed that the emulsion droplet size affects the particle size and macroscopic reaction rate during miniemulsion polymerization. A high-gravity emulsifier-free miniemulsion polymerization approach based on the use of a RPB reactor was proposed for the synthesis of PS nanodispersions. The use of a RPB reactor for miniemulsion polymerization could maintain the small size and size uniformity of emulsion droplets in the absence of surfactant. The PS nanoparticles obtained by high-gravity emulsifier-free miniemulsion polymerization exhibited an average

size of 71 nm with narrow size distribution and an average molecular weight 460,562 Da. Moreover, a unique phase separation phenomenon was observed in the styrene droplets during the miniemulsion polymerization process. Fluorescent nanoparticles doped with low-dose POSS-NH₂ on the surface were synthesized based on the phenomenon of phase separation, and their preliminary application for liquid marbles was demonstrated. This modification method could lead to tremendous molecular use efficiency in the surface modification field. Furthermore, the present work is anticipated to open a new avenue for the real-time tracking and characterization of reactions.

Declaration of Competing Interest

The authors have no conflicts to declare.

Acknowledgements

This work was supported by the National Key R&D Program of China (2017YFB0404405/2017YFB0404400) and National Natural Science Foundation of China (21622601). We are grateful to the “CHEMCLOUDCOMPUTING” of BUCT for computational support.

Appendix A. Supplementary material

Supplementary data to this article can be found online at <https://doi.org/10.1016/j.ces.2019.115288>.

References

- Alvim, H.H., Alecio, A.C., Vasconcellos, W.A., Furlan, M., de Oliveira, J.E., Saad, J.R.C., 2007. Analysis of camphorquinone in composite resins as a function of shade. *Dent. Mater.* 23, 1245–1249.
- Asua, J.M., 2014. Challenges for industrialization of miniemulsion polymerization. *Prog. Polym. Sci.* 39, 1797–1826.
- Becke, A.D., 1993. Density-functional thermochemistry. III. The role of exact exchange. *J. Chem. Phys.* 98, 5648–5652.
- Castor, C.A., Pontier, A., Durand, J., Pinto, J.C., Prat, L., 2015. Real time monitoring of the quiescent suspension polymerization of methyl methacrylate in microreactors—Part 1. A kinetic study by Raman spectroscopy and evolution of droplet size. *Chem. Eng. Sci.* 131, 340–352.
- Cook, W.D., 1992. Photopolymerization kinetics of dimethacrylates using the camphorquinone/amine initiator system. *Polymer* 33, 600–609.
- Delley, B., 2006. Ground-state enthalpies: evaluation of electronic structure approaches with emphasis on the density functional method. *J. Phys. Chem. A* 110, 13632–13639.
- Drache, M., Brandl, K., Reinhardt, R., Beuermann, S., 2018. Ab initio kinetic Monte Carlo simulation of seeded emulsion polymerizations of styrene. *PCCP* 20, 10796–10805.
- Fan, J.B., Song, Y.Y., Liu, H., Lu, Z.Y., Zhang, F.L., Liu, H.L., Meng, J.X., Gu, L., Wang, S.T., Jiang, L., 2017. A general strategy to synthesize chemically and topologically anisotropic Janus particles. *Sci. Adv.* 3.
- Fukui, T., Uchihashi, T., Sasaki, N., Watanabe, H., Takeuchi, M., Sugiyasu, K., 2018. Direct observation and manipulation of supramolecular polymerization by high-speed atomic force microscopy. *Angew. Chem.-Int. Ed.* 57, 15465–15470.
- Gharieb, A., Khoei, S., Mahdavian, A.R., 2019. Emulsion and miniemulsion techniques in preparation of polymer nanoparticles with versatile characteristics. *Adv. Colloid Interface Sci.* 269, 152–186.
- Guan, Weijiang, Wang, Si, Lu, Chao, Tang, Ben Zhong, 2016. Fluorescence microscopy as an alternative to electron microscopy for microscale dispersion evaluation of organic-inorganic composites. *Nat. Commun.* 7 (1). <https://doi.org/10.1038/ncomms11811>.
- Hans, M., Mourran, A., Henke, A., Keul, H., Moeller, M., 2009. Synthesis, characterization, and visualization of high-molecular-weight poly(glycidol-graft-epsilon-caprolactone) starlike polymers. *Macromolecules* 42, 1031–1036.
- He, X., Tang, R., Pu, Y., Wang, J.-X., Wang, Z., Wang, D., Chen, J.-F., 2019. High-gravity-hydrolysis approach to transparent nanozirconia/silicone encapsulation materials of light emitting diodes devices for healthy lighting. *Nano Energy* 62, 1–10.
- Hejmady, P., van Breemen, L.C.A., Anderson, P.D., Cardinaels, R., 2019. Laser sintering of polymer particle pairs studied by in situ visualization. *Soft Matter* 15, 1373–1387.
- Hong, Y.N., Lam, J.W.Y., Tang, B.Z., 2009. Aggregation-induced emission: phenomenon, mechanism and applications. *Chem. Commun.*, 4332–4353.
- Huang, C.J., Kobayashi, H., Moritaka, M., Okubo, M., 2017. Hollow particles are produced by the burying of sulfate end-groups inside particles prepared by emulsion polymerization of styrene with potassium persulfate as initiator in the absence/presence of a nonionic emulsifier. *Polym. Chem.* 8, 6972–6980.
- Huang, J., Wang, H., Yang, X., Quan, K., Yang, Y., Ying, L., Xie, N., Ou, M., Wang, K., 2016. Fluorescence resonance energy transfer-based hybridization chain reaction for in situ visualization of tumor-related mRNA. *Chem. Sci.* 7, 3829–3835.
- Jakubiak, J., Allonas, X., Fouassier, J.P., Sionkowska, A., Andrzejewska, E., Linden, L.A., Rabek, J.F., 2003. Camphorquinone-amines photoinitiating systems for the initiation of free radical polymerization. *Polymer* 44, 5219–5226.
- Jiang, Q.M., Huang, W.Y., Yang, H.J., Xue, X.Q., Jiang, B.B., Zhang, D.L., Fang, J.B., Chen, J.H., Yang, Y., Zhai, G.Q., Kong, L.Z., Guo, J.L., 2014. Radical emulsion polymerization with chain transfer monomer: an approach to branched vinyl polymers with high molecular weight and relatively narrow polydispersity. *Polym. Chem.* 5, 1863–1873.
- Landfester, K., 2009. Miniemulsion polymerization and the structure of polymer and hybrid nanoparticles. *Angew. Chem. Int. Ed.* 48, 4488–4507.
- Leung, C.W.T., Wang, Z.M., Zhao, E.G., Hong, Y.N., Chen, S.J., Kwok, R.T.K., Leung, A.C.S., Wen, R.S., Li, B.S., Lam, J.W.Y., Tang, B.Z., 2016. A lysosome-targeting AIEgen for autophagy visualization. *Adv. Healthcare Mater.* 5, 427–431.
- Liu, H., Hu, T., Wang, D., Shi, J., Zhang, J., Wang, J.-X., Pu, Y., Chen, J.-F., 2019. Preparation of fluorescent waterborne polyurethane nanodispersion by high-gravity miniemulsion polymerization for multifunctional applications. *Chem. Eng. Process. Process Intensification* 136, 36–43.
- Liu, S.J., Cheng, Y.H., Zhang, H.K., Qiu, Z.J., Kwok, R.T.K., Lam, J.W.Y., Tang, B., 2018. In situ monitoring of RAFT polymerization by tetraphenylethylene-containing agents with aggregation-induced emission characteristics. *Angew. Chem. Int. Ed.* 57, 6274–6278.
- Mei, J., Leung, N.L.C., Kwok, R.T.K., Lam, J.W.Y., Tang, B.Z., 2015. Aggregation-induced emission: together we shine, united we soar!. *Chem. Rev.* 115, 11718–11940.
- Neuville, A., Renaud, L., Luu, T.T., Minde, M.W., Jettstuen, E., Vinningland, J.L., Hiorth, A., Dysthe, D.K., 2017. Xurography for microfluidics on a reactive solid. *Lab. Chip* 17, 293–303.
- Pyun, J., Tang, C.B., Kowalewski, T., Frechet, J.M.J., Hawker, C.J., 2005. Synthesis and direct visualization of block copolymers composed of different macromolecular architectures. *Macromolecules* 38, 2674–2685.
- Qin, W., Ding, D., Liu, J.Z., Yuan, W.Z., Hu, Y., Liu, B., Tang, B.Z., 2012. Biocompatible nanoparticles with aggregation-induced emission characteristics as far-red/near-infrared fluorescent bioprobes for in vitro and in vivo imaging applications. *Adv. Funct. Mater.* 22, 771–779.
- Rao, J.P., Geckeler, K.E., 2011. Polymer nanoparticles: preparation techniques and size-control parameters. *Prog. Polym. Sci.* 36, 887–913.
- Sacci, R.L., Dudney, N.J., More, K.L., Parent, L.R., Arslan, I., Browning, N.D., Unocic, R. R., 2014. Direct visualization of initial SEI morphology and growth kinetics during lithium deposition by in situ electrochemical transmission electron microscopy. *Chem. Commun.* 50, 2104–2107.
- Sajjadi, S., Jahanad, F., 2006. Nanoparticle formation by highly diffusion-controlled emulsion polymerisation. *Chem. Eng. Sci.* 61, 3001–3008.
- Stephens, P.J., Devlin, F.J., Chabalowski, C.F., Frisch, M.J., 1994. Ab initio calculation of vibrational absorption and circular dichroism spectra using density functional force fields. *J. Phys. Chem.* 98, 11623–11627.
- Thickett, S.C., Teo, G.H., 2019. Recent advances in colloidal nanocomposite design via heterogeneous polymerization techniques. *Polym. Chem.*
- Tian, R., Li, K., Shi, W., Ding, C., Lu, C., 2019. In situ visualization of hydrophilic spatial heterogeneity inside microfluidic chips by fluorescence microscopy. *Lab. Chip* 19, 934–940.
- Truong, N.P., Quinn, J.F., Anastasaki, A., Rolland, M., Vu, M.N., Haddleton, D.M., Whittaker, M.R., Davis, T.P., 2017. Surfactant-free RAFT emulsion polymerization using a novel biocompatible thermoresponsive polymer. *Polym. Chem.* 8, 1353–1363.
- Wang, Z., Shi, J., Wang, D., Pu, Y., Wang, J.-X., Chen, J.-F., 2019. Metal-free catalytic oxidation of benzylic alcohols for benzaldehyde. *React. Chem. Eng.* 4, 507–515.
- Yuan, Y.Y., Kwok, R.T.K., Zhang, R.Y., Tang, B.Z., Liu, B., 2014. Targeted theranostic prodrugs based on an aggregation-induced emission (AIE) luminogen for real-time dual-drug tracking. *Chem. Commun.* 50, 11465–11468.
- Zhang, Y.-J., Bai, W.-Q., Wang, X.-L., Xia, X.-H., Gu, C.-D., Tu, J.-P., 2016. In situ confocal microscopic observation on inhibiting the dendrite formation of a-CNx/Li electrode. *J. Mater. Chem. A* 4, 15597–15604.
- Zhang, Y.L., Benes, N.E., Lammertink, R.G.H., 2015. Visualization and characterization of interfacial polymerization layer formation. *Lab. Chip* 15, 575–580.
- Zhao, Y.Y., Kwok, R.T.K., Lam, J.W.Y., Tang, B.Z., 2016. A highly fluorescent AIE-active theranostic agent with anti-tumor activity to specific cancer cells. *Nanoscale* 8, 12520–12523.